Guinier-Preston (GP) zone strengthening of dilute magnesium alloys comprised of earth-abundant elements

Jishnu J. Bhattacharyya[1*], Seth Faberman[2], Zehao Li[3], Aaron Sullivan[1], Du Cheng[1], Bassel Khoury[4], Yuanchen Gao[1], Taisuke Sasaki[3], Bicheng Zhou[1], Derek Warner[4,5], Sean R. Agnew[1]

1. Materials Science and Engineering, University of Virginia, Charlottesville, VA, U.S.A.
2. Mechanical and Aerospace Engineering, University of Virginia, Charlottesville, VA, U.S.A.
3. Research Center for Magnetic and Spintronic Materials, National Institute for Materials Science (NIMS), Tsukuba, JAPAN
4. School of Civil and Environmental Engineering, Cornell University, Ithaca NY 14853, USA
5. Canterbury Fracture Group, Civil and Natural Resources Engineering, University of Canterbury, Christchurch, 8041, New Zealand

Abstract

Dilute Mg alloys based upon earth abundant Al, Zn, and Ca (along with minor additions of Mn and Zr) exhibit attractive combinations of strength, ductility, and workability via high-speed extrusion. These alloys derive their strength from high number densities of ordered, single atomic layer Guinier-Preston (GP) zones. The present study explores the potential of two quaternary Mg-Zn-Ca-Zr (ZXK210 and ZXK310) alloys produced as sheet materials. The anisotropic plastic responses of the two alloys are described using an elastoplastic self-consistent (EVPSC) polycrystal plasticity model. Similar to what was observed in AXM alloys with Mg-Ca-Al GP zones, prismatic slip is more potently strengthened than basal slip. The Mg-Zn-Ca GP zones are found to be intrinsically stronger and have a higher antiphase domain boundary energy than the Mg-Al-Ca GP zones. Finally, it is shown that the ZXK alloys are immune from natural over-aging.

Keywords: strength modeling, age-hardening, crystal plasticity, GP zone

* Corresponding author: jjb4cp@virginia.edu

Age-hardenable Mg alloys based upon dilute additions of earth abundant elements Ca, Al and/or Zn have been developed with attractive combinations of strength, ductility, and workability via high-speed extrusion [1–4]. These dilute Mg alloys are strengthened by a high number density of disc-shaped GP zones lying on the basal plane [1,3]. The precise structure of the Mg-Zn-Ca GP zones was recently revealed by cluster expansion methods [5]. A recent study has determined the distinct strengthening effect of these GP zones on the different slip and twinning modes in the Mg-Al-Ca-Mn alloy, AXM10304 [6]. It was shown that basal slip and extension twinning modes are only modestly strengthened by the GP zones, as compared to the prismatic slip. This interpretation also served to explain why rolled sheet products are less potently strengthened than extruded, even though the GP zone number densities are essentially the same in the two product forms [7]. A polycrystal plasticity-based approach is employed to assess the strengthening effect of GP zones in another class of dilute alloys which contains Zn.

Mg alloys ZXK210 (Mg-1.6Zn-0.5Ca-0.5Zr, in wt. %) and ZXK310 (Mg-3.0Zn-0.5Ca-0.5Zr, in wt. %) were cast, homogenized and rolled, as detailed in [8]. Tensile specimens of gage length 20 mm and width 4 mm were electro-discharge machined from the as-rolled sheets with loading axis parallel to the rolling direction (RD), transverse direction (TD) and at 45° to RD towards TD (henceforth referred to as 45). The solution treatment (SS) was carried out in a box furnace, in air, at 450±2 °C for 1 h followed by water quench. Subsequently, some of these solutionized materials were aged at 200±5 °C for 0.5h, 2h, and 72h. The age hardening response was measured by a Vickers hardness tester (Tinius Olsen FH14) under 0.1 kgf load with 10s dwell time. Prior to hardness testing, ~14 mm size coupons were ground to 1200 grit finish using SiC paper. Measurements from 10 indents were averaged to obtain the mean hardness for each heat treatment condition. In general, the samples were tested within one week of the heat treatments, however, in order to examine the possibility of natural (i.e. room temperature) aging of the solutionized material and natural over-aging of the peak-aged (PA) materials, the samples were left at ambient conditions and hardness tested periodically, over the course of a year. Room temperature tensile tests were performed with an initial strain rate of 10^{-3} s^{-1}. Some of the tensile specimens were deformed up to 9% strain while others were strained up to failure. Square pieces of ~ 25 mm side, ground to midplane (between 0.4-0.6 mm of the 1 mm thick sheet) up to 1200 grit finish using SiC paper, were used for X-ray diffraction-based texture measurements, as described elsewhere [6,9]. An Elasto-ViscoPlastic Self-Consistent (EVPSC) polycrystal plasticity code based on the

formulation of Molinari et al. [10,11] and Wang et al., [12] is employed to parse the effects of strengthening obstacles on individual deformation modes.

To characterize the previously observed Zn-Zr particles [8,13] with tetragonal structure similar to Zn_2Zr_3 observed in the Mg-Zn-Zr ternary system [14], TEM/STEM foils extracted from the solutionized material were electropolished with the same electrolyte as in [8], at 90V and -50°C, yielding ~11 mA/mm^2. Imaging of GP zones and the Zn-Zr particles were performed using FEI-Titan G^2 and Themis-Z operating 200 kV. EELS measurement was used to assess foil thickness. ImageJ software was used to post-process micrographs to obtain the particle number density and size distribution (see Supplement). Electron density functional theory (DFT) was used as in [5,15] to determine formation energy, lattice constants, and elastic properties of the Zn-Zr phases as well as the antiphase boundary energy (APBE) of the Mg-Zn-Ca GP zone (see Supplement).

Fig. 1 shows the age hardening curves of ZXK210 and ZXK310 alloys during isothermal aging at 200 ºC. The '0' curve corresponds to measurements performed within one week of the heat treatment. The other curves correspond to measurements made 1.5, 4 (6 for ZXK310) and 11 months after the heat treatment, during which the samples were naturally aging at ambient. The ZXK210 alloy has a hardness of 56±3 HV in the solutionized condition, which increases to 69±3 HV after aging for 0.5 h, and to 66±3 HV after aging for 2 h. Upon further aging for 72 h, the hardness decreases to 59±2 HV (Fig. 1a). An increase in Zn content from 1.6 to 3 wt.% has little effect on the hardness of the aged material (Fig 1b). The age-hardening kinetics also remains unaffected, where the peak hardness is reached after 0.5 h. Note, the age hardening response of quaternary ZXK210 has been assessed at 170°C and that of the ternary Mg-1.6Zn-0.5Ca alloy has been assessed at 200°C [8] (Fig. 1a). It is evident that the aging kinetics is slower at 170°C, and the peak hardness of 66.1±1.5 HV is reached after 4 h. The value of the peak hardness is essentially the same as that obtained after aging at 200 °C, and addition of Zr also has negligible effect on the age hardening behavior. When natural aging is considered, all except the solutionized condition show essentially no evolution in hardness; i.e. the values fall within 4 HV which is comparable to the level of experimental uncertainty. The solutionized material naturally ages with time and the hardness increases by ~7 HV for ZXK210 and by ~10 HV for ZXK310 (Fig. 1c).

Solution heat treatment results in a weak basal texture (~3 mrd) where the basal poles are tilted ~30°-50° towards TD and the $(10\bar{1}0)$ prismatic poles are weakly aligned with RD (Fig. S4). This texture is similar to that observed in Mg-Zn-RE alloys [16] and other Ca containing alloys [17]. A

comprehensive description of microstructure evolution and detailed precipitate structure characterization of ZXK210 and ternary Mg-Ca-Zn is given in [8,15]. In brief, an equiaxed microstructure with average grain size of 6.6±2.8 μm is observed after SS. TEM characterization revealed mostly spherical Zn-Zr particles in the solutionized material (Fig. 2a), which remain present in all aging conditions. It is assumed that these are the Zn_2Zr_3 phase introduced previously [13,14]. There are occasional, isolated rod-shaped particles which tend to be rich in Zn and Ca. The peak-aged material contains GP zones which are monolayered thin discs, on the basal planes of the Mg matrix (Fig. 2b). For ZXK210, aged at 170°C-4 h, the average diameter, D, of the GP zones is 3.2 ± 0.4 nm and the number density, N_v, as obtained from 3D APT data is 9.9×10^{23} m^{-3}. For the ternary Mg-1.6Zn-0.5Ca, aged at 200°C-0.3 h, D of the GP zones is ~3.5 nm and N_v is 1.22×10^{24} m^{-3} (Table 1). Thus for the present case of ZXK210 aged at 200°C, the average of the abovementioned microstructure data is used for subsequent calculations (Table 1). Note, these values are similar to that observed in the AXM alloy [6]. Interestingly, upon further aging the hardness hardly changes indicating that the commensurate change in D and N_v must cancel one another. Finally, the composition of the matrix in the solutionized and peak-aged conditions are also obtained from the APT data [8]. Since the solutionized material exhibited some evidence of natural aging (Fig. 1c), tensile tests were performed after one year of natural aging, but no evidence of strengthening was observed (Fig. S5). Perhaps the larger strain response or other deformation modes probed by hardness testing are altered whereas in-plane tensile yielding is not.

The experimental and simulated flow curves for various aging conditions of ZXK210 (Fig. 3) and ZXK310 (Fig. S6) show that the strength and the strain hardening anisotropy are well-described by the model. The best-fit Voce parameters for the two alloys, for different aging conditions, are shown in Table 2. For both alloys, RD is stronger than TD and the fact that the simulations capture this anisotropy confirms that the initial texture of the materials is responsible. Also captured by the simulation, the strength of the samples oriented 45° from RD lies intermediate to RD and TD. The tensile response of both alloys reveal the same trend as the age hardening curves. The solutionized and overaged materials have similar strength, and ZXK310 is stronger than ZXK210 in the solutionized condition, due to higher solute content. Interestingly, the strength of the two alloys is similar after 0.5/2 h aging, and the same Voce parameters adequately model these aging conditions of both alloys (Table 2). As noted for hardness, aging at 170 °C results in similar strength, albeit the peak-aged condition is reached more slowly, after 4 h [8].

The polycrystal model enables determination of strength increment due to the GP zones, $\Delta\tau^{\alpha}_{EVPSC} = \tau^{\alpha}_{0}(PA) - \tau^{\alpha}_{0}(SS)$ for each deformation mode, α, via the strategy employed previously for AXM alloy [6]. For in-plane tension of basal textured sheets, yielding is mainly controlled by the basal and the prismatic slip of <a> dislocations, accompanied by some tensile twinning, but not pyramidal slip of <c+a> dislocations. Examining the detailed effects of the GP zones on deformation twinning is beyond the scope of the present work; however, since the initial texture favors some twining activity when strained in tension along TD, an estimate of the strengthening can be inferred from $\Delta\tau$ (Table 3). Only a moderate strength increment is observed, which is in agreement with that observed for the AXM alloys, as well as previous observations that fine precipitates have only a nominal effect on strengthening the deformation twinning mode in Mg alloys. For ZXK210, basal and prismatic slip modes are strengthened to a similar extent as was observed for the AXM alloy. ZXK310, on the other hand, shows a lower strengthening effect, perhaps because of a lower number density of GP zones, which merits further investigation. The CRSS, τ^{α}_{0}, of each mode involves contributions from intrinsic lattice resistance, τ^{α}_{l}, solute atoms, $\Delta\tau^{\alpha}_{s}$, grain boundaries, $\Delta\tau^{\alpha}_{HP}$, forest dislocations, $\Delta\tau^{\alpha}_{f}$, and precipitates. $\Delta\tau^{\alpha}_{f}$ is negligible for this heat-treated material. For instance, a typical initial dislocation density, ρ = 1x10^{12} m^{-2}, yields a contribution ~1 MPa, via the Taylor relation, $\Delta\tau^{\alpha}_{f} = \beta\mu b^{\alpha}\sqrt{\rho}$ ($\beta \sim 0.3, \mu$ is shear modulus, b^{α} is Burgers vector of <a> dislocations). Therefore, the yield strength is expressed as: $\tau^{\alpha}_{0}(PA) = \tau^{\alpha}_{l} + \Delta\tau^{\alpha}_{HP} + \Delta\tau^{\alpha}_{s} + \sqrt{{\Delta\tau^{\alpha}_{GP}}^{2} + {\Delta\tau^{\alpha}_{sph}}^{2}}$, where $\Delta\tau^{\alpha}_{GP}$ is contribution from GP zones and $\Delta\tau^{\alpha}_{sph}$ is contribution from Zn-Zr precipitates, and a Pythagorean superposition principle is employed. For the solutionized material, where GP zones are absent, the CRSS simplifies to: $\tau^{\alpha}_{0}(SS) = \tau^{\alpha}_{l} + \Delta\tau^{\alpha}_{HP} + \Delta\tau^{\alpha}_{s} + \Delta\tau^{\alpha}_{sph}$.

τ^{α}_{l} and $\Delta\tau^{\alpha}_{HP}$ are assumed to remain unchanged among different aging conditions. The changes in $\Delta\tau^{\alpha}_{s}$ between the solutionized and peak-aged tempers are also revealed to be negligible. For instance, the APT data show that the solute concentrations in the matrix decrease from (in at%) 0.41±0.02 to 0.20±0.01 for Zn and 0.24±0.02 to 0.11±0.01, for Ca, while the Zr concentration of 0.001 at% in the matrix is not observed to change with aging [8]. These changes in solute content are predicted to induce a change of <2 MPa in the strength of basal slip [18]. Complex solute softening (at low temperatures) and strengthening effects on prismatic slip due to dilute Ca and Zn additions have been observed experimentally [19] and computationally [20]. However, only

modest (within the range of uncertainty) effects are observed at ambient temperatures justifying the present first-order approximation of no solute effect on prismatic slip. The Zn-Zr precipitates have a log-normal size distribution with an average particle size, d = 20 nm, and number density, N_v = 7.5×10^{20} m^{-3}. Based on this microstructure, the crystal structure [21], and high stiffness coefficients of the Zn_2Zr_3 phase [see Supplement], it is expected that the dislocations will rather bow around than shear them. Thus, the resulting strengthening contribution of 15 MPa may be considered as an upper bound estimate.

The strength increment due to shearable obstacles is obtained from the Friedel-Fleischer relation [22–24], $\Delta\tau = \left(\frac{F}{2T}\right)^{\frac{3}{2}}\left(\frac{2T}{bl_{ppt}}\right)$, where l_{ppt} is the interparticle spacing. The force to overcome the obstacle, $F = \chi\mu b r_p$; where r_p is the mean particle radius on the slip plane and χ is a parameter indicative of the intrinsic resistance of the obstacle. Assuming line tension, $T \cong \frac{1}{2}\mu b^2$, yields $\Delta\tau = \left(\frac{\chi r_p}{b}\right)^{3/2}\left(\frac{\mu b}{l_{ppt}}\right)$. Using EVPSC results, the strength increment of slip mode α due to the GP zones: $\Delta\tau_{GP}^{\alpha} = \sqrt{\left(\Delta\tau_{EVPSC}^{\alpha} + \Delta\tau_{sph}^{\alpha}\right)^2 - \Delta\tau_{sph}^{\alpha\,2}}$ which reveals that prismatic slip is strengthened ~2.5 times more than the basal slip, similar to that observed in the AXM alloy. Interestingly, the geometric factor $\left(\frac{r_p{}^{3/2}}{l_{ppt}}\right)$ for these *shearable* basal discs causes basal slip to be more potently strengthened than prismatic [25–27]. Therefore, the distinction in the *intrinsic resistance* of these GP zones must be responsible for the observed effect.

Using $\Delta\tau_{GP}^{\alpha}$ and the microstructure data from Table 1, the ratio of the intrinsic resistance, χ, can be estimated as: $\frac{\chi_{prism}}{\chi_{basal}} \approx \left(\frac{r_{p-basal}}{r_{p-prism}}\right)\left(\frac{\Delta\tau_{prism}\times l_{ppt-prism}}{\Delta\tau_{basal}\times l_{ppt-basal}}\right)^{\frac{2}{3}} = 2.6 \pm 0.6$. This relative strengthening effect on the basal and the prismatic <a> slip modes is intrinsic and not due to precipitate shape which would induce an opposite effect (Table 1). The passage of dislocations parallel to the zone (basal slip) offers a lower resistance compared to shearing perpendicular to the zone (prismatic slip) by a factor which is very similar to that for the AXM alloys.

Note, however, that the intrinsic strength of the Mg-Zn-Ca GP zone is 1.6 ± 0.4 times greater than the Mg-Al-Ca GP zone (Table 1). It was initially hypothesized that the strengthening was due to anti-phase domain boundary (APB) formation due to the passage of the shearing dislocation (Fig. 4). DFT estimates (Table 3) reveal that the APBE of the Mg-Zn-Ca GP zone is

1.7 times greater than the Mg-Al-Ca GP zone, and thus quantitatively correlates with the above estimate of the intrinsic strengths. In both instances, the APBE-based estimates of the strength increment are lower than those estimated based upon polycrystal plasticity modeling (48 and 46 MPa for ZXK210 and AXM10304, respectively). This suggests that other mechanisms, e.g., modulus mismatch, coherency strains, or perhaps the details of the Generalized Stacking Fault Energy (GSFE) curves may be required to explain the total strengthening effect, but these results suggest that the sum of these other contributions are similar between the two alloys.

Finally, it is noted that the force required for the dislocation to overcome these GP zones via prismatic slip is modest (Table 3). To put these results in context, clusters at early stages of precipitation in AA6xxx have a similar critical bowing angle θ_c~165°, (F = 0.28 nN, $\frac{F}{2T} = 0.13$) [28] while the strengthening precipitates of similar size in maraging steels impart a rather high resisting force of ~2 nN $\left(\frac{F}{2T} = 0.38\right)$ [29]. Nevertheless, their high number density enables attractive levels of strength to be obtained with little impact upon tensile ductility, which may be due to GP zones dissolution by the dislocations during deformation [30,31] rather than damage nucleation in addition to the previously noted impact upon strain rate sensitivity [32].

Acknowledgements: This work is supported by the U.S. National Science Foundation DMREF grant CMMI-1921926. B. Khoury & D. Warner acknowledges the support by the U.S. National Science Foundation grant #1922081. Z. Li & T. Sasaki would like to acknowledge financial support from JSPS KAKENHI [Grant Number JP21H01675], the Light Metal Educational Foundation, Inc., and Element Strategy Initiative of MEXT [Grant Number JPMXP0112101000]. The authors would like to thank the University of Virginia Nanomaterials Characterization Facility and Dr. Helge Heinrich for their assistance in TEM sample preparation and characterization.

Author Contribution

Jishnu J Bhattacharyya - conceptualization, data curation, formal analysis, investigation, methodology, software, validation, visualization, and writing—original draft. **Seth Faberman** - formal analysis, investigation, visualization. **Zehao Li** - formal analysis, investigation. **Aaron Sullivan** - formal analysis, investigation, visualization, writing—review & editing. **Du Cheng** - formal analysis, investigation, visualization. **Bassel Khoury** - formal analysis, investigation,

visualization, writing—review & editing. **□uan□hen □ao** - formal analysis, investigation, visualization, writing—review & editing. **□aisu□e Sasa□i** - funding acquisition, resources, supervision, and project administration. **Bi□heng Zhou** - funding acquisition, resources, supervision, and project administration. **Dere□ □ arner** - funding acquisition, resources, supervision, and project administration. **Sean □□Agne□** - conceptualization, writing—review & editing, funding acquisition, resources, supervision, and project administration.

□e□eren□es

[1] K. Hono, C.L. Mendis, T.T. Sasaki, K. Oh-Ishi, Towards the development of heat-treatable high-strength wrought Mg alloys, Scr. Mater. 63 (2010) 710–715. https://doi.org/10.1016/j.scriptamat.2010.01.038.

[2] J. Jayaraj, C.L. Mendis, T. Ohkubo, K. Oh-Ishi, K. Hono, Enhanced precipitation hardening of Mg-Ca alloy by Al addition, Scr. Mater. 63 (2010) 831–834. https://doi.org/10.1016/j.scriptamat.2010.06.028.

[3] T. Nakata, C. Xu, R. Ajima, K. Shimizu, S. Hanaki, T.T. Sasaki, L. Ma, K. Hono, S. Kamado, Strong and ductile age-hardening Mg-Al-Ca-Mn alloy that can be extruded as fast as aluminum alloys, Acta Mater. 130 (2017) 261–270. https://doi.org/10.1016/j.actamat.2017.03.046.

[4] M. Cihova, R. Schäublin, L.B. Hauser, S.S.A. Gerstl, C. Simson, P.J. Uggowitzer, J.F. Löffler, Rational design of a lean magnesium-based alloy with high age-hardening response, Acta Mater. 158 (2018) 214–229. https://doi.org/10.1016/j.actamat.2018.07.054.

[5] D. Cheng, E.R. Hoglund, K. Wang, J.M. Howe, S.R. Agnew, B.C. Zhou, Atomic structures of ordered monolayer GP zones in Mg-Zn-X (X= Ca, Nd) systems, Scr. Mater. 216 (2022) 114744. https://doi.org/10.1016/j.scriptamat.2022.114744.

[6] J.J. Bhattacharyya, T. Sasaki, T. Nakata, K. Hono, S. Kamado, S.R.; Agnew, Determining the strength of GP zones both parallel and perpendicular to the zone, Acta Mater. 171 (2019) 231–239.

[7] J.J. Bhattacharyya, T.T. Sasaki, T. Nakata, S.R. Agnew, Why rolled Mg-Al-Ca-Mn alloys are less responsive to aging as compared to the extruded, Scr. Mater. 233 (2023) 115513. https://doi.org/10.1016/j.scriptamat.2023.115513.

[8] Z. Li, Development of Heat-treatable Wrought Magnesium Alloys with Excellent Formability, PhD dissertation, 2021.

[9] J.J. Bhattacharyya, S.R. Agnew, G. Muralidharan, Texture enhancement during grain growth of magnesium alloy AZ31B, Acta Mater. 86 (2015) 80–94. https://doi.org/10.1016/j.actamat.2014.12.009.

[10] A. Molinari, G.R. Canova, S. Ahzi, A Self Consistent Approach of the Large Deformation polycrystal viscoplasticity, Acta Metall. 35 (1987) 2983–2994. https://doi.org/10.1016/0001-6160(87)90297-5.

[11] A. Molinari, S. Ahzi, R. Kouddane, On the self-consistent modeling of elastic-plastic behavior of polycrystals, Mech. Mater. 26 (1997) 43–62. https://doi.org/10.1016/S0167-6636(97)00017-3.

[12] H. Wang, P.D. Wu, C.N. Tomé, Y. Huang, A finite strain elastic-viscoplastic self-consistent

model for polycrystalline materials, J. Mech. Phys. Solids. 58 (2010) 594–612. https://doi.org/10.1016/j.jmps.2010.01.004.
[13] X. Gao, B.C. Muddle, J.F. Nie, Transmission electron microscopy of Zr-Zn precipitate rods in magnesium alloys containing Zr and Zn, Philos. Mag. Lett. 89 (2009) 33–43. https://doi.org/10.1080/09500830802524096.
[14] Y.P. Ren, Y. Guo, D. Chen, S. Li, W.L. Pei, G.W. Qin, Isothermal section of MgZnZr ternary system at 345 ° C, Calphad Comput. Coupling Phase Diagrams Thermochem. 35 (2011) 411–415. https://doi.org/10.1016/j.calphad.2011.05.009.
[15] Z.H. Li, D. Cheng, K. Wang, E.R. Hoglund, J.M. Howe, B.C. Zhou, T.T. Sasaki, T. Ohkubo, K. Hono, Revisited precipitation process in dilute Mg-Ca-Zn alloys, Acta Mater. 257 (2023). https://doi.org/10.1016/j.actamat.2023.119072.
[16] L.W.F. Mackenzie, M.O. Pekguleryuz, The recrystallization and texture of magnesium-zinc-cerium alloys, Scr. Mater. 59 (2008) 665–668. https://doi.org/10.1016/j.scriptamat.2008.05.021.
[17] Z.R. Zeng, Y.M. Zhu, S.W. Xu, M.Z. Bian, C.H.J. Davies, N. Birbilis, J.F. Nie, Texture evolution during static recrystallization of cold-rolled magnesium alloys, Acta Mater. 105 (2016) 479–494. https://doi.org/10.1016/j.actamat.2015.12.045.
[18] J.A. Yasi, L.G. Hector, D.R. Trinkle, First-principles data for solid-solution strengthening of magnesium: From geometry and chemistry to properties, Acta Mater. 58 (2010) 5704–5713. https://doi.org/10.1016/j.actamat.2010.06.045.
[19] A. Akhtar, E. Teghtsoonian, Solid solution strengthening of magnesium single crystals—ii the effect of solute on the ease of prismatic slip, Acta Metall. 17 (1969) 1351–1356. https://doi.org/10.1016/0001-6160(69)90152-7.
[20] J.A. Yasi, L.G. Hector, D.R. Trinkle, Prediction of thermal cross-slip stress in magnesium alloys from a geometric interaction model, Acta Mater. 60 (2012) 2350–2358. https://doi.org/10.1016/j.actamat.2012.01.004.
[21] https://next-gen.materialsproject.org/materials/mp-1207421?formula=Zn2Zr3#crystal_structure, (n.d.).
[22] V. Gerold, Precipitation hardening, Dislocations in Solids. 4 (1980) 219–260.
[23] A.. Ardell, Precipitation Hardening, Metall. Trans. A. 16 (1985) 2131–2165.
[24] A.S. Argon, Strengthening mechanisms in crystal plasticity, Oxford: Oxford University Press., 2008.
[25] F. Wang, J.J. Bhattacharyya, S.R. Agnew, Effect of precipitate shape and orientation on Orowan strengthening of non-basal slip modes in hexagonal crystals, application to magnesium alloys, Mater. Sci. Eng. A. 666 (2016) 114–122. https://doi.org/10.1016/j.msea.2016.04.056.
[26] J.J. Bhattacharyya, F. Wang, N. Stanford, S.R. Agnew, Slip mode dependency of dislocation shearing and looping of precipitates in Mg alloy WE43, Acta Mater. 146 (2018) 55–62. https://doi.org/10.1016/j.actamat.2017.12.043.
[27] J.F. Nie, Effects of precipitate shape and orientation on dispersion strengthening in magnesium alloys, Scr. Mater. 48 (2003) 1009–1015. https://doi.org/10.1016/S1359-6462(02)00497-9.
[28] R.K.W. Marceau, A. De Vaucorbeil, G. Sha, S.P. Ringer, W.J. Poole, Analysis of strengthening in AA6111 during the early stages of aging: Atom probe tomography and yield stress modelling, Acta Mater. 61 (2013) 7285–7303. https://doi.org/10.1016/j.actamat.2013.08.033.

[29] W.W. Sun, R.K.W. Marceau, M.J. Styles, D. Barbier, C.R. Hutchinson, G phase precipitation and strengthening in ultra-high strength ferritic steels: Towards lean 'maraging' metallurgy, Acta Mater. 130 (2017) 28–46. https://doi.org/10.1016/j.actamat.2017.03.032.
[30] Stephen Niezgoda, Personal Communication, (2024).
[31] J. Miao, F. Xue, T. Liu, T. Avey, E.A. Marquis, A.A. Luo, Achieving high strength-ductility synergy via Guinier-Preston zone formation in a new Mg–Zn–Al–Ca–Mn–Ce sheet alloy, Mater. Sci. Eng. A. 901 (2024) 146586. https://doi.org/10.1016/j.msea.2024.146586.
[32] J.J. Bhattacharyya, T. Nakata, S. Kamado, S.R. Agnew, Origins of high strength and ductility combination in a Guinier-Preston zone containing Mg-Al-Ca-Mn alloy, Scr. Mater. 163 (2019) 121–124. https://doi.org/10.1016/j.scriptamat.2019.01.013.

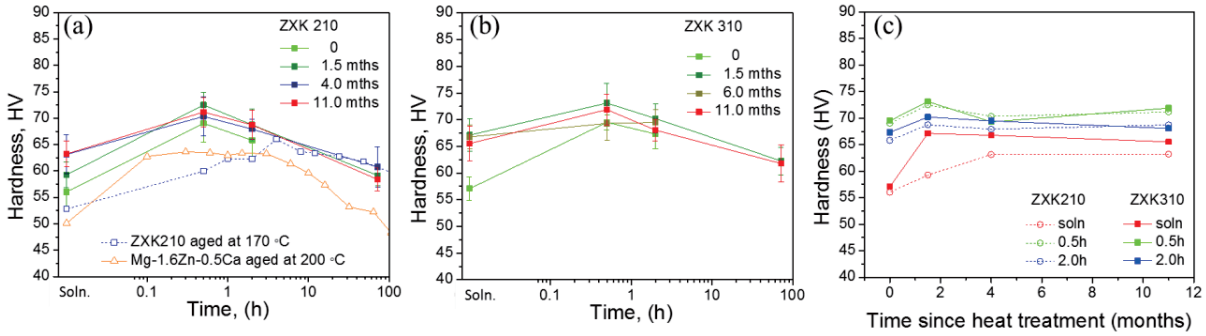

Fig. 1 Variations in Vickers hardness as a function of aging time for a) ZXK210, and b) ZXK310, measured within one week (denoted by '0') and several months after the heat treatment was performed. Age hardening data for ZXK210 aged at 170 °C and the ternary alloy Mg-1.6Zn -0.5Ca aged at 200 °C are also shown [8]. c) The variation in hardness as a function of time elapsed since the heat treatment was performed indicating the level of natural aging at ambient.

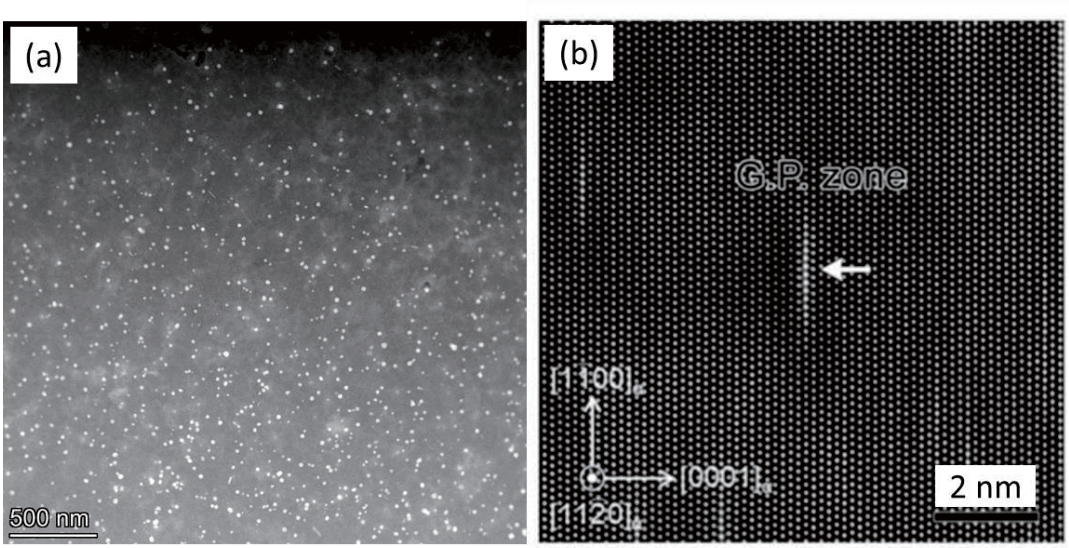

Fig. 2 (a) HAADF-STEM micrograph obtained from the solutionized ZXK210 alloy showing the Zn-Zr particles. (b) Atomic resolution HAADF-STEM micrograph from the peak-aged (170 °C/4 h) ZXK210 alloy, acquired along the $[11\bar{2}0]_{Mg}$, showing monolayer G.P. zones which appear as bright single columns lying on the $(0001)_{Mg}$ planes.

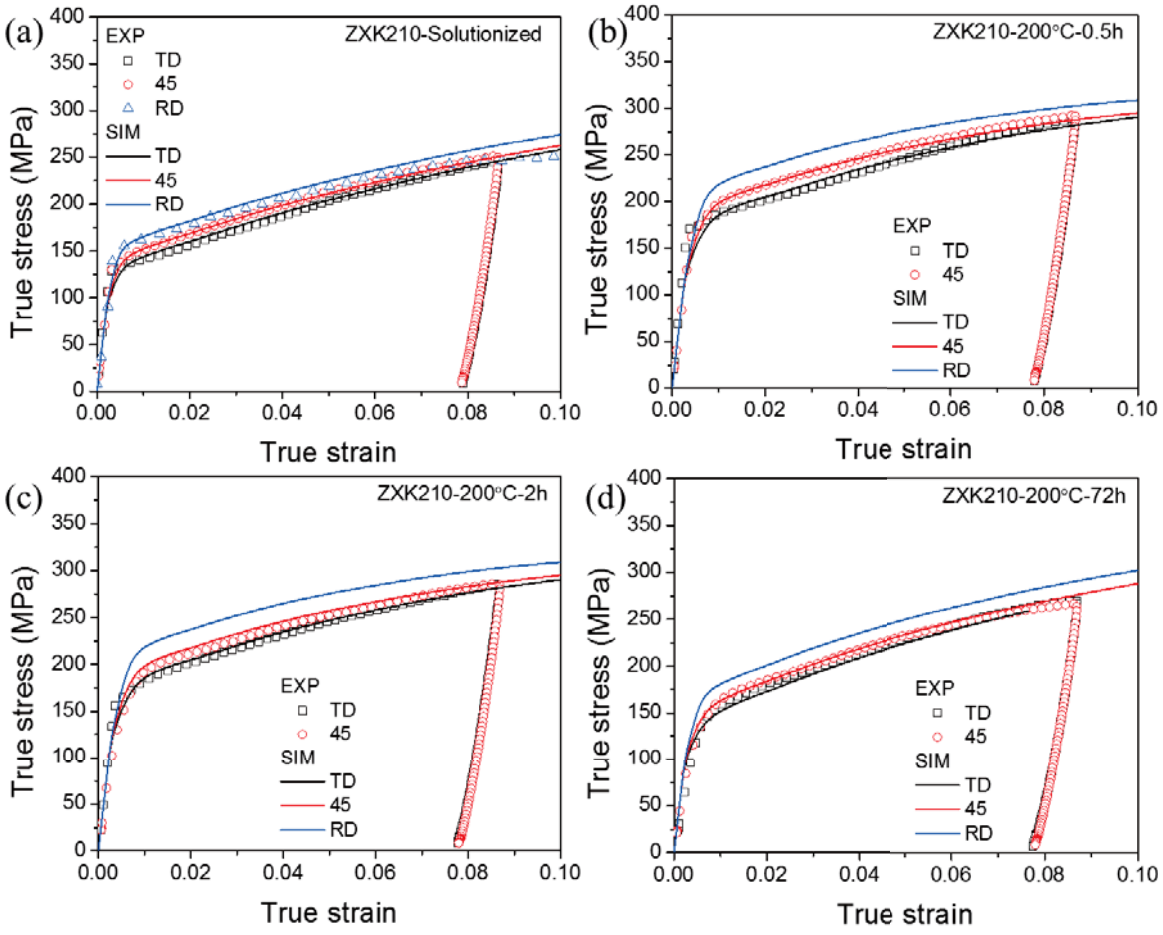

Fig. 3 The experimental and simulated flow curves of ZXK210 alloy for various aging conditions.

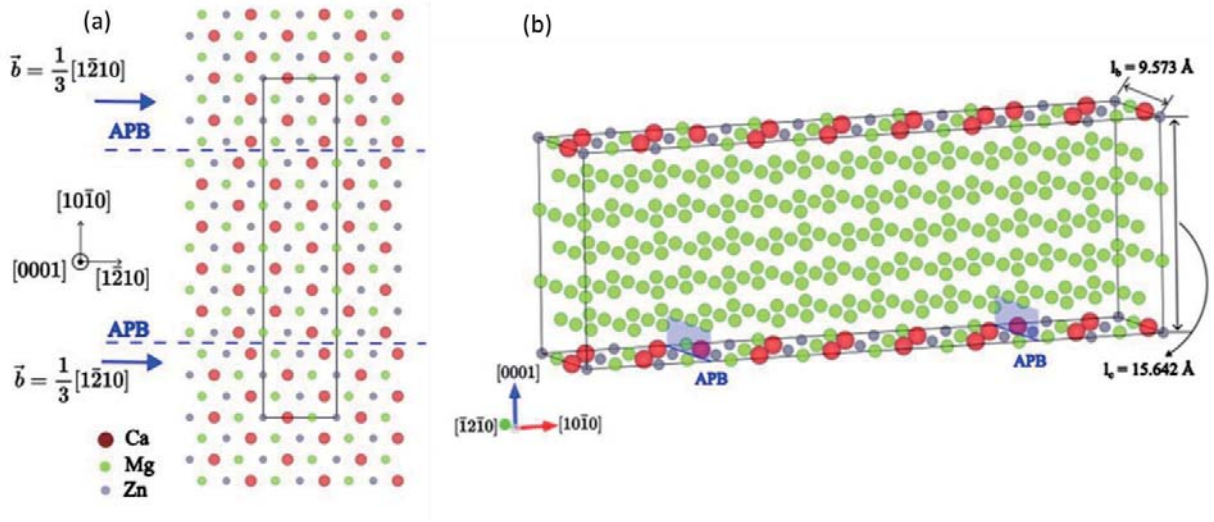

Fig. 4 Illustration of the APB generated by $\frac{1}{3}[1\bar{2}10]$ Burgers vector in the monolayer Mg-Ca-Zn GP zone. (a) Projection of monolayer GP zone with APBs (indicated by blue dash lines) on the (0001) plane. Green, red and grey circles represent Mg, Ca and Zn atoms, respectively. (b) Unit cell with APBs (indicated by blue solid lines) used in the current DFT work. The bottom layer simulates the monolayer GP zone with APB, and the remaining five layers simulate the HCP Mg matrix. The blue rectangle indicates the prismatic slip plane.

Table(s)

Table 1: Number density N_v, volume fraction f_v, and the size of the GP zones obtained by averaging the data for ZXK210 aged at 170 °C-4h and for the ternary Mg-1.6Zn-0.5Ca alloy aged at 200 °C-0.3h. The resulting mean planar diameter D_p, radius r_p, interparticle spacing l_{ppt}, the geometric factor $\frac{{r_p}^{3/2}}{l_{ppt}}$ and the intrinsic strength χ for basal and prismatic slip modes based on the averaged data, are also shown.

	N_v ($\times 10^{23}$ m^{-3})	f_v (%)	D_p ($\times 10^{-9}$ m)	t_p ($\times 10^{-9}$ m)	r_p ($\times 10^{-9}$ m)	l_{ppt} ($\times 10^{-9}$ m)	$\frac{{r_p}^{3/2}}{l_{ppt}}$ ($\times 10^{-6}\sqrt{m}$)	χ
Basal	11.1 ± 0.7	0.5±0.1	D = 3.4±0.4	0.51	$\frac{D_p}{2}$ = 1.68 ± 0.2	$\frac{1}{\sqrt{tN_v}} - D$ = 38.9 ± 1.5	1.8 ± 0.3	0.05 ± 0.01
Prism			$\frac{\pi}{4}D$ = 2.6±0.3	0.51	$\frac{\sqrt{D_p t_p}}{2}$ = 0.58 ± 0.03	$\frac{1}{\sqrt{DN_v}} - \frac{\pi}{4}D$ = 13.8 ±1.3	1.0 ± 0.1	0.14 ± 0.02

Table 2: Best-fit Voce hardening parameters for ZXK210 and ZXK310 alloys for the solutionized (SS), peak-aged (PA), and over-aged (OA) conditions.

		ZXK210					**ZXK310**			
		τ_0	τ_1	θ_0	θ_1		τ_0	τ_1	θ_0	θ_1
Solution treated (SS)	prismatic	85	60	200	0		100	120	200	0
	basal	30	30	200	0		35	35	200	0
	c+a	*280*	*250*	*500*	*0*		*280*	*250*	*500*	*0*
	ttw	35	0	50	50		40	0	1	1
0.5h/2h (PA)	prismatic	120	20	200	0		120	20	200	0
	basal	40	10	200	0		40	10	200	0
	c+a	*280*	*250*	*500*	*0*		*280*	*250*	*500*	*0*
	ttw	45	0	25	25		45	0	25	25
72 h (OA)	prismatic	100	60	200	0		115	40	200	0
	basal	30	30	200	0		35	10	200	0
	c+a	*280*	*250*	*500*	*0*		*280*	*250*	*500*	*0*
	ttw	35	0	100	100		35	0	25	25

Table 3: A comparison among three alloys, ZXK210, ZXK310, and AXM100. The differences in CRSS for basal and prismatic slip mode , $\Delta\tau$, as obtained from EVPSC model parameters, the strength contribution , $\Delta\tau_{sph}^{\alpha}$, due to the Zn-Zr particles for ZXK alloys and Al-Mn particles for AXM100, the strengthening contribution of the GP zones, $\Delta\tau_{GP}$, the ratio of the intrinsic shear resistance of the prismatic to basal slip, $\frac{\chi_{prism}}{\chi_{basal}}$, the APB energies, γ_{APB}, the resulting strength increment due to APBE, $\Delta\tau_{APB}$, the force required to overcome the obstacle, *F*, and the critical bowing angle θ_c. The values of $\Delta\tau$, $\Delta\tau_{sph}^{\alpha}$, $\Delta\tau_{GP}^{\alpha}$ and $\frac{\chi_{prism}}{\chi_{basal}}$ for AXM100 (in grey table cells) are obtained from reference [6].

	ZXK210			**ZXK310**			**□X□ 00**		
	Basal	Prism	TTW	Basal	Prism	TTW	Basal	Prism	TTW
$\Delta\tau = \tau_0^{\alpha}(PA) - \tau_0^{\alpha}(SS)$	10	35	10	5	20	5	10	39	15
$\Delta\tau_{sph}^{\alpha}$	15	15	-	15	15	-	7.7	7.7	-
$\Delta\tau_{GP}^{\alpha}$	20	48	-	13	31	-	16	46	
$\frac{\chi_{prism}}{\chi_{basal}}$	2.6 ± 0.6			2.6			2.9 ± 1.2		
γ_{APB} (mJm^{-2})	175 ± 9			-			104 ± 5		
$\Delta\tau_{APB} = \frac{\gamma_{APB}}{2b}\left(\frac{D_p}{l_{ppt}} - f_v\right)$ (MPa)	21 ± 3			-			20 ± 7		
□(nN)	0.43			-			0.33		
$\frac{F}{2T}$	0.24			-			0.19		
θ_c (°)	152			-			159		